Engineering Surface Oxophilicity of Copper for Electrochemical CO2 Reduction to Ethanol

Minhan Li
Donghua University

Nan Song
East China University of Science and Technology

Fangzhou Zhang
Donghua University

Wei Luo
Donghua University

Jun Chen
University of Wollongong   https://orcid.org/0000-0003-2218-7382

Wan Jiang
Donghua University

Jianping Yang (✉ zcjpyang@gmail.com)
Donghua University   https://orcid.org/0000-0003-1495-270X

Abstract

Copper-based materials is known for converting CO_2 into deep reduction products via electrochemical reduction reaction (CO_2RR). As the major multicarbon products (C_{2+}), ethanol (C_2H_5OH) and ethylene (C_2H_4) are believed to share a common oxygenic intermediate according to theoretical studies, while the key factors that bifurcate C_2H_5OH and C_2H_4 pathways on Cu-based catalysts are not fully understood. Here, we propose a surface oxophilicity regulation strategy to enhance C_2H_5OH production in CO_2RR, demonstrating by a Cu-Sn bimetallic system. Compared with bare Cu catalyst, the Cu-Sn bimetallic catalysts show improved C_2H_5OH but suppressed C_2H_4 selectivity. The experimental results and theoretical calculations demonstrate that the surface oxophilicity of Cu-Sn catalysts plays an important role in steering the protonation of the key oxygenic intermediate and guides the reaction pathways to C_2H_5OH. This study provides new insights into the electrocatalyst design for enhanced production of oxygenic products from CO_2RR by engineering the surface oxophilicity of copper-based catalysts.

Introduction

The electrochemical CO_2 reduction reaction has been attracting worldwide attention due to its great potential to convert CO_2 and H_2O into valuable chemicals using renewable power. [1, 2] CO_2 is a stable and inert molecule, which makes it essential to develop highly efficient catalysts to lower the energy barrier of CO_2RR process.[3, 4] Cu-based materials stands out as a unique kind of catalysts because of their unique selectivity toward multi-carbon (C_{2+}) products.[5, 6] Extensive efforts have been made to increase the FE of total C_{2+} products.[7] As the major C_{2+} products, C_2H_4 and C_2H_5OH are both 12-electron transfer products while C_2H_5OH usually exhibits lower selectivity than C_2H_4 on Cu-based catalysts in neutral electrolyte of CO_2RR.[8] Ethanol is an important liquid fuel with high energy density (26.8 MJ/kg). To enhance the production of C_2H_5OH from CO_2RR, several strategies have been proposed, such as tandem effect,[9] electronic effect,[10] strain effect,[11] adsorbed hydrogen assistance,[12] and binding site diversification.[8]

Although the pathways for the formation of C_2H_4 and C_2H_5OH have not reached a consensus, both theoretical and experimental researches have proposed that the formation of C_2H_4 and C_2H_5OH branch after CO dimerization and they share a key oxygenic species.[10, 13−16] This adsorbed specie can be referred as the selectivity-determining intermediate (SDI), whose next proton and electron transfer bifurcates the pathways for C_2H_4 and C_2H_5OH.[10, 14, 17] The surface oxophilicity has been found to play a key role in tuning the binding strength of the oxygenic intermediates and thereby affecting the activity and selectivity of many O-bond relevant electrocatalytic processes, such as hydrogen evolution reaction (HER), oxygen evolution reaction (OER), oxygen reduction reaction (ORR), and ethanol oxidation reaction (EOR).[18−20] For CO_2RR process, the oxophilicity of Cu-based catalysts has also been found to play a key role in promoting carbonyl-containing products and branching the reaction pathway toward hydrocarbons and oxygenic products.[21, 22] Recently, a catalyst contains dual active sites was proposed to enhance the

production of C_2H_5OH by introducing strong oxophilic nitrogen-doped graphene.[23] Therefore, regulating the surface oxophilicity of Cu-based catalysts holds the promise to enhance C_2H_5OH production in CO_2RR. However, the way to efficiently regulate the surface oxophilicity of Cu-based catalysts is still lacking and how the surface oxophilicity affect the selectivity of C_2 products in CO_2RR remains unclear.

Bimetallic strategy that combines two elements with different oxophilicity is a promising way to regulate the oxophilicity of metal-based catalysts.[24, 25] According to the oxophilicity of the metals reflected by the bond dissociation enthalpies of metal-oxygen (Figure S1),[26, 27] Sn is a wise choice to couple with Cu because of the greater oxophilicity of Sn and the formate selectivity of Sn in CO_2RR.[28] The Cu-Sn bimetallic catalysts have been extensively investigated in CO_2RR and exhibited high activity and selectivity of two-electron (2e) products (Table S1) at low and moderate overpotentials (From − 0.5 to -1.1 V_{RHE} in literatures).[29−32] Although some studies have suggested small amount of deep reduction products were generated on Cu-Sn bimetallic catalysts at moderate overpotentials,[33, 34] the CO_2RR performance of Cu-Sn bimetallic catalysts at large overpotentials remains unexplored.

In this study, we focus on the influence of surface oxophilicity of Cu-based catalysts on CO_2RR performance. To regulate the surface oxophilicity of Cu, a series of dendrite Cu-Sn bimetallic catalysts is synthesized by a facile replacement method, featuring surface-enriched Sn incorporated in Cu lattice. Compared to Cu, the Cu-Sn bimetallic catalysts exhibited enhanced C_2H_5OH selectivity but suppressed C_2H_4 selectivity at relatively large overpotential. The effects of Sn modification on the oxophilicity and C_2 products pathways on $CuSn_x$ catalysts were studied by both experiments and theoretical calculations. An insightful understanding of the effect of surface oxophilicity on C_2H_5OH selectivity in CO_2RR was proposed, suggesting the surface oxophilicity regulation of Cu-based catalysts is a promising way to promote C_2H_5OH production in CO_2RR.

Results And Discussion

Synthesis and characterization of $CuSn_x$

The Cu-Sn bimetallic catalysts were synthesized by a rapid and facile method that based on simultaneous galvanic replacement reactions (Figure S2a). Driven by the difference in the redox potential, this galvanic replacement process is a powerful method for fabricating dendritic structures with controllable chemical composition.[35] Once a piece of cleaned Zn foil was added into a mixed solution containing Cu^{2+}, Sn^{2+} and HCl, the surface of silver gray Zn foil turned into black immediately, indicating the reaction took place rapidly (Figure S2b). The Zn foil almost disappeared and the color of the solution became light after 1 hour, indicating the deposition of Cu and Sn as well as the dissolution of Zn^{2+}. The obtained solid products were emersed in diluted HCl solution and then washed with deionized water repeatedly to remove the superfluous Zn. The X-ray diffraction (XRD) patterns of $CuSn_x$ catalysts with x ≤ 0.10 showed similar diffraction peaks with bare Cu catalyst while no crystalline Sn species were

detected (Figure S3a). As seen in Fig. 1a, with the increasing content of Sn, all the diffraction peaks shifted to lower 2θ angle and the peaks became widened, indicating the enlarged lattice spacing and decreased crystallinity and grain size.[29] These results are likely due to the Sn atoms with larger atomic radius than Cu atoms are highly dispersed in the lattice of Cu, which will be further discussed below.[36] Furthermore, the XRD pattern of $CuSn_{0.25}$ catalyst showed that the intermetallic phase corresponding to $Cu_{41}Sn_{11}$ emerged when the Sn content further increased to 25% (Figure S3b)

The morphologies of the $CuSn_x$ bimetallic catalysts were first characterized by scanning electron microscope (SEM). For comparison, bare Cu sample was also prepared by the same method without Sn^{2+} addition. The bare Cu counterpart exhibited irregular rod-like morphology (Figure S4a). Interestingly, with only small amount of Sn addition, the microstructure of $CuSn_{0.01}$ catalysts changed drastically and exhibited typical dendritic morphology (Fig. 1b), indicating that Sn^{2+} ions may facilitate the formation of dendritic morphology in the replacement process. With the increasing Sn content, the dendrite surfaces became coarsening and small grains emerge (Figure S4). The dendrite structure is beneficial to CO_2RR process by lowering the charge transfer resistance and enhancing the mass transfer.[34, 37] Representative high-resolution transmission electron microscope (HR-TEM) images showed good crystalline of $CuSn_{0.01}$ catalyst (Figure S5b). The zoomed-in edge of $CuSn_{0.01}$ catalyst exhibited distorted lattice fringe, which is likely due to the heteroatomic doping of Sn in Cu lattice (Fig. 1c). The elemental mapping of $CuSn_{0.01}$ catalyst showed the predominant Cu and highly scattered Sn elements were uniformly distributed in the catalyst (Fig. 1d). On the other hand, the TEM images of $CuSn_{0.10}$ catalyst showed that the coarsened dendrite surface become assembly of small particles and a distinct amorphous layer of about 5 nm formed on the catalyst surface(Figure S6a-c). The elemental mapping of $CuSn_{0.10}$ catalyst showed a uniform distribution of both Cu and Sn elements (Figure S6d-g). The double layer capacities of the $CuSn_x$ catalysts were then measured to determine the electrochemical surface area (ECSA). Compared to bare Cu, the introduction of Sn increased the ECSAs of the $CuSn_x$ catalysts (Figure S7). The $CuSn_x$ catalysts exhibited similar ECSA except for $CuSn_{0.25}$, which may be due to the severe coarsening of $CuSn_{0.25}$.

The X-ray photoelectron spectroscopy (XPS) measurement was then carried out to investigate the surface properties of $CuSn_x$ catalysts. The Cu $2p_{1/2}$ and Cu $2p_{3/2}$ peaks of the $CuSn_x$ catalysts located at 952.4 eV and 932.5 eV, respectively, which can be assigned to either Cu^0 or Cu^{1+} (Fig. 1e). The Cu LMM Auger electron spectra suggested that Cu^{1+} was the main Cu species in bare Cu catalysts due to the spontaneous oxidation under ambient condition. However, with the increasing Sn content in $CuSn_x$, the valance of Cu gradually shifted to metallic Cu^0, which is likely due to the stronger O affinity of Sn than Cu (Fig. 1f). The doublet peaks of Sn 3d (Fig. 1g) that can be assigned to the $3d_{3/2}$ and $3d_{5/2}$ peaks centered at 494.6 and 486.3 eV was in between the peaks of Sn^{2+} and Sn^{4+}, indicating the oxidation state of $Sn^{\delta+}$ in the $CuSn_x$ catalysts. The peak shift for both Cu and Sn demonstrated the electronic interaction between incorporated Sn and Cu matrix in the $CuSn_x$ catalysts. Furthermore, a small peak at about 485.0 eV that assigned to metallic Sn^0 in Sn $3d_{5/2}$ peak (493.2 eV for Sn $3d_{3/2}$ peak) appeared in $CuSn_{0.10}$ and

$CuSn_{0.25}$ catalysts. The composition of the $CuSn_x$ catalysts was characterized by both energy dispersive spectroscopy (EDS) and XPS. Given the nanoscale of the $CuSn_x$ catalysts, the Cu/Sn ratios determined by EDS reflects the bulk composition of the catalysts, which were close to the designed values (Fig. 1h). However, the surface and subsurface Cu/Sn ratio in depth of a few nanometers determined by XPS measurements were quite different from the EDS results. The Cu/Sn ratio in the $CuSn_x$ catalysts decreases in the order: surface (XPS) > subsurface (XPS after Ar sputtering) > > bulk (EDS). These results indicate that the Sn species enriched in the surface of the dendrite $CuSn_x$ catalysts, which is crucial for the catalytic reaction.[33]

CO$_2$RR performance

The CO_2RR performance of the dendrite $CuSn_x$ catalysts were evaluated in a H-cell divided by a Nafion membrane. The total FEs of all products on different $CuSn_x$ catalysts were in the range of 93–101% (Figure S8). The FEs of different reduction products are plotted against potentials to show the change of product distributions with $CuSn_x$ catalysts (Fig. 2 and Figure S9). The competing HER was largely suppressed for all the $CuSn_x$ catalysts at the tested potentials apart from only a few exceptions at -0.7 V_{RHE} (Figure S9a). As reported by many previous studies, the introduction of Sn greatly improved the selectivity of Cu-based catalysts and CO became the major reduction product at low and moderate overpotentials.[32] Among all the $CuSn_x$ catalysts, $CuSn_{0.01}$ exhibited the highest FE of 96.4% for CO with a partial current density of 6.50 mA/cm^2 at -0.8 V_{RHE} (Fig. 2a and Figure S10b). The FEs of CO decreased gradually with the increasing Sn content and the maximum FEs of CO for $CuSn_{0.025}$, $CuSn_{0.05}$, $CuSn_{0.10}$, and $CuSn_{0.25}$ were 80.6%, 71.7%, 59.8%, and 53.7%, respectively. As another 2e transfer products, the FEs of formate increased with the increasing Sn content in $CuSn_x$ catalysts, which is due to the surface-enriched Sn and the high formate-producing activity of Sn in CO_2RR (Fig. 2b). As mentioned before, the suppressed HER and enhanced 2e products (CO and formate) have been extensively observed and discussed by many studies on bimetallic Cu-Sn catalysts. Sn metal possess a weaker H affinity than Cu metal and SnO_2 modification was reported to lower the H_2 chemisorption of CuO.[32, 38] Therefore, it is commonly accepted that the surface decorated Sn atoms on Cu disfavor the adsorption of *H and thereby suppress the HER.[37, 39] Meanwhile, the formation of the important *COOH intermediate is facilitated, while the adsorption of CO is either weakened or unaffected by the combination of Cu and Sn.[30, 31, 39] Therefore, the enhanced production of 2e products is usually reported in previous studies about Cu-Sn bimetallic catalysts. Similarly, A recent study showed that $Cu_{99}Sn_1$ catalyst with only 1% of Sn exhibited a high CO selectivity over 90% while $Cu_{70}Sn_{30}$ catalyst exhibited a high formate selectivity at low and moderate overpotentials.[33]

We then continued the CO_2RR tests at more negative potentials where deep reduction products are generated. The bare Cu catalyst exhibited the highest FEs and current densities of C_2H_4 in the whole potential range (Fig. 2c and e). Clearly, the formation of C_2H_4 on Cu catalysts was suppressed by Sn

modification. With the increasing Sn content in $CuSn_x$ catalysts, not only the FEs of C_2H_4 decreased, but also the onset potentials for C_2H_4 formation lowered. The onset potentials of C_2H_5OH on the $CuSn_x$ catalysts were also lower than that on the bare Cu catalyst. However, the FEs of C_2H_5OH on $CuSn_{0.01}$, $CuSn_{0.025}$ and $CuSn_{0.05}$ catalysts were higher than that on Cu catalyst at potentials below − 1.2 V_{RHE} (Fig. 2d and Figure S11). The highest FE of C_2H_5OH reached 25.93% on $CuSn_{0.025}$ at -1.4 V_{RHE} with a large partial current density of 15.05 mA/cm^2 (Fig. 2d and f). Previous studies of Cu-Sn bimetallic catalysts for CO_2RR always exhibited high FEs for CO or formate at potentials higher than − 1.1 V_{RHE} (Table S1).[30, 33] Herein, it was found that C_2H_4 activity was suppressed while C_2H_5OH production was boosted at relatively large overpotentials on our $CuSn_x$ catalysts.

Bifurcation between C_2H_4 and C_2H_5OH

To gain further insight into the selectivity trend of C_2H_4 and C_2H_5OH on $CuSn_x$ catalysts, the FE ratios of C_2H_5OH/C_2H_4 of different $CuSn_x$ catalysts were compared at the potentials ranging from − 1.1 V_{RHE} to -1.4 V_{RHE} (Figure S12). Obviously, the FE ratios of C_2H_5OH/C_2H_4 of the $CuSn_x$ catalysts were higher than that of the bare Cu catalyst and showed good linearity against the surface Sn/Cu ratio ($CuSn_{0.25}$ catalyst was not included in Fig. 3a since the deviation is relatively large, which is likely due to its low FEs for both C_2H_4 and C_2H_5OH). To understand the unusual C_2 products selectivity, we first sought mechanistic insight into the bifurcation between C_2H_4 and C_2H_5OH. Although the pathways for the formation of C_2H_4 and C_2H_5OH have not reached a consensus, it has been evidenced by experimental and theoretical results that C_2H_4 and C_2H_5OH products branch after C-C coupling.[4, 16] Koper and co-workers have previously shown that H_2C-CHO^* is the selectivity-determining intermediate (SDI) that bifurcating C_2H_4 and C_2H_5OH.[14] The hydrogenation of C_α in H_2C-CHO^* leads to H_3C-CHO^*, which is further reduced to C_2H_5OH. On the contrary, the hydrogenation of C_β forms $H_2C-CH_2O^*$, which leads the formation of C_2H_4.[10, 17] Based on these previous studies, we carried out theoretical calculation of the Gibbs free energy of these two pathways. Given the feature of incorporated Sn in $CuSn_x$ and the high C_2 selectivity of Cu(100) facet, slab models of Sn substituted Cu(100) facets were built and Sn-Cu(100) slab was selected for free energy calculation (Figure S13). As seen in Fig. 3b and c, on Cu(100), the energy barriers for C_2H_4 and C_2H_5OH pathways were 1.54 eV and 1.77 eV respectively, suggesting the C_2H_4 formation is thermodynamically more favorable. In contrast, the energy barrier of C_2H_5OH pathway was 0.22 eV lower than that of C_2H_4 pathway on Sn-Cu(100). The calculation results revealed that the C_2H_5OH pathway on Cu sites was enhanced by Sn modification, which is in accordance with the FEs trends.

In the whole potential range, the introduction of Sn into Cu significantly improved the production of CO, which is believed to be the key intermediate for C-C coupling. The enhancement of local CO concentration could facilitate C_{2+} production via tandem effect on bimetallic catalysts.[40] However, the reversed selectivity tendencies of C_2H_4 and C_2H_5OH in this work ruled out the tandem effect in our $CuSn_x$ catalysts. The surface oxophilicity of catalysts is of great importance for the processes that involves

oxygen relevant species, such as *O, *OH, and adsorbed oxygenic intermediates.[28, 41, 42] The binding strength of O bonded SDI of C_2H_4 and C_2H_5OH could be influenced by the oxophilicity of the binding sites.[23, 26] To this end, we first tried to understand how the surface oxophilicity changed with the component of the $CuSn_x$ catalysts. To accomplish that, cyclic voltammetry (CV) tests in 0.1 M NaOH solution were performed to determine the binding strength of adsorbed hydroxide ions (OH_{ad}) on the $CuSn_x$ catalysts, which reflects their oxophilicity.[42, 43] As depicted in Fig. 4a, the CV curve of bare Cu catalyst showed Cu^0-Cu^{1+} redox peaks at around 328.6 and 577.7 mV_{RHE}.[44] In addition, a peak associated with the adsorption of OH_{ad} appeared at around 360 mV_{RHE} (OH_{ad}-I).[44] The zoomed-in OH_{ad}-I peaks on bare Cu catalyst exhibited typical OH_{ad} peaks obtained on polycrystalline Cu, where a strong OH_{ad} peak corresponding to Cu(100) is at 359.1 mV_{RHE}, followed by two weak OH_{ad} peaks assigned to Cu(110) and Cu(111) (Fig. 4b).[45, 46] The introduction of Sn altered the adsorption behavior of OH_{ad}-I on Cu sites. On the $CuSn_x$ catalyst, there was only a strong OH_{ad}-I peak that shifted to more negative potentials, indicating the enhanced adsorption strength of OH_{ad} (Fig. 4d and Figure S14).[42] The adsorption strength of OH_{ad}-I reached the maximum on $CuSn_{0.025}$ catalyst, on which the onset and vertex of OH_{ad}-I peak negatively shifted to 343.1 and 352.4 mV_{RHE}, indicating the strongest oxophilicity of Cu sites on $CuSn_{0.025}$ (Fig. 4d).[45] With the increasing Sn content in the $CuSn_x$ catalysts, the intensity of OH_{ad}-I peak decreased and an additional broad peak at around 150 mV_{RHE} (OH_{ad}-II) appeared on $CuSn_{0.05}$ and $CuSn_{0.10}$ catalysts (Figure S14b-d). Given the stronger O affinity of Sn than Cu, the intensified OH_{ad}-II peak with the increasing Sn content should be assigned to the strong adsorption of OH_{ad} sites of Sn. For $CuSn_{0.25}$ catalyst, only a broad peak at 100 ~ 200 mV_{RHE} could be observed, indicating that strong adsorption of OH_{ad} on Sn sites prevailed when the surface is abundant in Sn (Figure S4d and h). These results demonstrate that the introduction of Sn on Cu surface enhances the oxophilicity of the $CuSn_x$ catalysts in two ways: 1) enhanced oxophilicity of Cu sites; 2) creation of new stronger oxophilic Sn sites.

Based on the above results, we tried to elucidate the importance of surface oxophilicity to C_2H_5OH production in CO_2RR. The FEs of C_2H_5OH at -1.3 and − 1.4 V_{RHE} on the $CuSn_x$ catalysts were plotted against the vertex potentials of OH_{ad}-I peaks in the CV curves, which reflects the surface oxophilicity of the $CuSn_x$ catalysts (Fig. 4e). The great linearity strongly supported the positive correlation between the oxophilicity of the Cu sites and C_2H_5OH production (Bare Cu and $CuSn_{0.25}$ catalysts are not included in Fig. 4e because the multiple OH_{ad}-I peaks in bare Cu catalyst and the indiscernible OH_{ad}-I peak in $CuSn_{0.25}$ catalyst). We then sought theoretical calculation for understanding the effects of oxophilicity on the SDI. As seen in Fig. 4f, the stable SDI bonded to Cu sites on both Cu(100) and Sn-Cu(100) and the calculated adsorption energy were − 1.77 eV and − 1.85 eV respectively, indicating the enhanced oxophilicity of Cu sites could stabilize the adsorption of SDI. As discussed above, the next proton and electron transfer step of the SDI bifurcates the C_2H_4 and C_2H_5OH pathways. The charge analysis of adsorbed SDI showed that the C_α carried less positive charge and the C_β also carried less negative charge

on Sn-Cu(100), which both contribute the next protonation on C_β to be easier on Sn-Cu(100). Therefore, we believe that the enhanced oxophilicity of Cu sites in $CuSn_x$ catalysts stabilize the SDI and affect its protonation to facilitate the C_2H_5OH pathway in CO_2RR.

To further verify the effect of surface oxophilicity on CO_2RR, we combined Cu with Pb due to its modest oxophilicity between Cu and Sn and suitable redox property (Figure S15). The $CuPb_{0.025}$ catalyst was prepared by the same method and their CO_2RR performance were tested at -0.7 to -1.3 V_{RHE}. The $CuPb_{0.025}$ catalyst exhibited a higher FE of C_2H_5OH than bare Cu catalyst. Although its FEs of C_2H_5OH were not as high as $CuSn_{0.025}$, the FEs of C_2H_4 for $CuPb_{0.025}$ was comparable or even superior to bare Cu catalyst and the maximum FEs of C_{2+} for $CuPb_{0.025}$ reached 70.78% at -1.2 V_{RHE}. We then synthesized $CuAg_{0.025}$ bimetallic catalyst by the similar method as Ag possesses lower oxophilicity than Cu (Figure S16). Both the FEs of C_2H_4 and C_2H_5OH on $CuAg_{0.025}$ catalyst was lower than that on bare Cu catalyst. These results strongly support the surface oxophilicity regulation strategy for improving C_2H_5OH production in CO_2RR. Interestingly, there was no $n-C_3H_7OH$ product that could be detected on $CuAg_{0.025}$ catalyst at any potentials, while a new doublet assigned to H in acetaldehyde emerged in the ^1H NMR patterns (Figure S16f). Although the mechanism of the acetaldehyde formation is rarely reported, it is believed that acetaldehyde formed on the C_2H_5OH pathway.[47] Such interesting selectivity behaviors of $CuPb_{0.025}$ and $CuAg_{0.025}$ catalysts imply that the effect of surface oxophilicity cannot be accomplished alone without other effects in bimetallic catalysts, such as electronic and strain effects.[11, 21] Therefore, it is believed that this strategy can cooperate with other ways that facilitate the C-C coupling, such as tandem effect and Cu^1-Cu^0 synergistic effect,[6, 40] to further increase the production of C_{2+} oxygenic products in CO_2RR.

Conclusion

In summary, we have proposed the surface oxophilicity regulation strategy to improve C_2H_5OH production in CO_2RR via steering the absorbed SDI. A series of $CuSn_x$ bimetallic catalysts featured typical dendrite microstructure with surface-enriched Sn species dispersed in Cu matrix were synthesized. The $CuSn_x$ catalysts exhibited enhanced CO_2RR to 2e products at low and moderate overpotentials, while high FE of C_2H_5OH and increased C_2H_5OH/C_2H_4 ratio were achieved at large overpotentials. It was found that the introduction of Sn atom on Cu surface could enhance the surface oxophilicity of the catalysts, which play a key role in bifurcating the reaction pathways between C_2H_4 and C_2H_5OH by steering the protonation of the key oxygenic intermediate. Based on the above experimental and theoretical results, we believe that the surface oxophilicity regulation of of Cu-based catalysts is a promising strategy to design highly efficient electrocatalysts for oxygenic products in CO_2RR.

Methods

Materials synthesis

Firstly, a piece of Zn foil (1 cm*1 cm* 0.1 mm) was sonicated in water, ethanol, and acetone for 30 min, respectively. Then 10 mL of mixed metal ions solution containing certain amount of $CuCl_2 \cdot 2H_2O$ and $SnCl_2 \cdot 2H_2O$ in 100 mM HCl. The total concentration of metal ions was 100 mM. Then the cleaned Zn foil was immersed in 0.1 M HCl for 5 min to remove the surface oxide layer before immersing into above solution. After 1h of replacement reaction at room temperature, the reaction was stopped by pouring out the solution. To remove the surplus Zn metal completely, the Cu-Sn dendrite deposition was then washed with diluted HCl solution (0.1 M) and then washed with ethanol three times by centrifugation. The obtained product was dried under vacuum and denoted as $CuSn_x$ catalysts (x stands for the Sn content in the metal ion solution, which is 0.01, 0.025, 0.05, 0.10, and 0.25 in this work assuming total metal ions is 1). The $CuSn_x$ catalysts were stored under inert atmosphere in a glove box ($O_2 < 0.1$ ppm, $H_2O < 0.1$ ppm).

$CuPb_{0.025}$ and $CuAg_{0.025}$ was synthesized by the similar method to $CuSn_{0.025}$. The metal ions solution for the synthesis of $CuPb_{0.025}$ contains 100 mM of $Cu(NO_3)_2 \cdot 3H_2O$ and $Pb(CH_3COO)_2$. For the synthesis of $CuAg_{0.025}$, ammonia water was added drop by drop into a solution of 10 mL containing 0.975 mmol $Cu(NO_3)_2 \cdot 3H_2O$ and 0.025 mmol $AgNO_3$ under ultrasonic until the initially formed precipitate was just dissolved, forming a dark blue solution. Then 100 mg Mg powder was added into this solution and left still for 1 h. The obtained solid was filtered and washed with 0.1 M HCl solution until no bubbles appeared. Finally, the product was washed with deionized water for 5 times and dried under vacuum at room temperature.

Electrode preparation

1 mg of as-prepared $CuSn_x$ catalysts and 0.2 mg of carbon black were dispersed in 190 uL methanol. Subsequently, 10uL of Nafion (5 wt.%) was added, followed by ultrasonication for at least 1h. Then 6 uL catalyst ink was dropped onto a L-type glass carbon electrode with a diameter of 4 mm (geometric area: ~ 0.1256 cm^2) using a pipette and dried under ambient air. The catalyst loading was about 0.24 mg•cm^{-2}. The catalysts were electrochemically activated in CO_2-saturated 0.1 M $KHCO_3$ solution by CV (10 scans) from – 0.5 to -1.5 V_{RHE}.

Electrochemical measurements

CO_2 electrolysis was carried out in a gas-tight, custom-made two-compartment cell, in which the working electrode was separated from the counter electrode by a Nafion 117 membrane. Ag/AgCl (saturated KCl) was used as the reference electrode and the three-electrode set-up was connected to a potentiostat (Biologic VMP3). A 0.1 M $KHCO_3$ electrolyte solution was used for all CO_2RR tests and the electrolyte in the cathodic compartment was stirred at a constant rate of 500 rpm during electrolysis. Before CO_2RR, the catholyte were bubbled with CO_2 (99.99%) for 20–30 min to reach saturation, and CO_2 was kept purging into the cathodic compartment at flow-rate of 20 sccm during the CO_2RR. To determine the FEs of the reduced products, chronoamperometry was performed for 1 hour at iR-corrected potentials.

All potentials were measured against an Ag/AgCl reference electrode (saturated KCl) and converted to the reversible hydrogen electrode (RHE) scale by

$$E_{RHE} = E_{Ag/AgCl} + 0.198 + 0.059 \times pH$$

All the potentials in the text were iR-corrected. The resistance between the reference and working electrodes was measured by Potential Electrochemical Impedance Spectroscopy (PEIS) and 80% of the ohmic drop was compensated automatically by software and the rest 20% remained uncompensated. Generally, the value of uncompensated resistance (Ru) determined by PEIS was about 110−115 Ω in CO_2 saturated 0.1 M $KHCO_3$ in this work.

The CV tests were carried out in Ar-saturated 0.1 M NaOH solution. The working electrode were prepared by the same method as for the chronoamperometry tests and electrochemically activated in CO_2-saturated 0.1 M $KHCO_3$ solution by CV (10 scans) from − 0.5 to -1.5 V_{RHE} before CV tests in alkaline solution. The scan rate was 10 mV/s and the potential range was 0 to 0.8 V_{RHE} (-0.2 to 0.8 V_{RHE} for $CuSn_{0.25}$).

Materials characterization

SEM images were obtained using field emission scanning electron microscope of TESCAN MAIA3 with EDS of Bruker Quantax 200 XFlash. TEM images were acquired using FEI Talos F200S. HAADF-STEM and elemental mapping analysis were performed on FEI Talos F200S. Powder XRD was obtained using Bruker D2 Phaser. XPS measurements were performed on Escalab 250Xi and Ar sputtering was carried out at 1000 eV for 300 seconds. ^{1}H NMR spectra was obtained on Bruker AVANCE III 600MHz nuclear magnetic resonance spectrometer.

Calculation details

The Vienna ab initio simulation package (VASP) code was used for DFT calculations in this work with projected augmented wave (PAW) pseudopotential to approximate the interaction between ion cores and valence electrons. A plane wave cutoff energy of 400 eV was chosen, together with Perdew-Burke-Ernzerhof (PBE) method as the exchange-correlation functional. A Monkhorst−Pack mesh of 5×5×1 k-points was used for the Brillouin zone integration. A force convergence of 0.03 eV/ Å was used in geometry optimization.

The optimum lattice parameters of the Cu unit cell were calculated to be a = 3.631 Å, close to the experimental values of 3.615 Å. The Cu(100) surface was modeled using a p (3×3) supercell with five-layer slab, the Cu(110) surface was modeled using a p (3×2) supercell with seven-layer slab, and the Cu(111) surface was modeled using a p (2×2) supercell with five-layer slab. The bottom two layers were fixed at the bulk lattice position. A 15 Å-vacuum layer was employed to separate the surface from the periodic image in the direction along the surface of the slab. The energy of adsorption (E_{ads}) were calculated using $E_{ads} = E_{complex} − (E_{adsorbate} + E_{surface})$, where $E_{complex}$ represents the energy of adsorbate

on the Cu(100) surface, $E_{adsorbate}$ and $E_{surface}$ are the energies of isolated adsorbate and on Cu(100) surface, respectively.

Gas product analysis

Gas products from the cathodic compartment during CO_2RR were analyzed using a GC-2014 (Shimadzu) equipped with a TCD detector and two FID detectors, one of which was coupled with a methanizer to detect low concentration of CO. High purity Ar (99.999%) was used as the carrier gas. The gas products, including H_2, CO, CH_4 and C_2H_4 were calibrated using standard mixed gases with different content (Dalian Special Gases Co., LTD) and the calibration curves was shown in Figure S17.

The Faradaic efficiencies of the gas products were calculated by the GC data using the following equation:

$$FE_g = \frac{Q_g}{Q_{total}} \times 100\% = \frac{\frac{v}{60s/min} \times \frac{y}{24.5L/mol} \times n \times F}{j_{average}} \times 100\%$$

where v is gas flow rate measured by a flowmeter, which is 10.0 sccm for all the tests. y is the measured volumetric content of the gas product. n is the number of electrons required to form the gas products, and n = 2, 2, 8, and 12 for H_2, CO, CH_4, and C_2H_4, respectively. F is the Faraday constant (96485 C/mol). j is the average current density.

Liquid product analysis

Liquid products were analyzed by a 600 MHz NMR spectrometer (Bruker Avance 3 HD 600 MHz) using a presaturation technique to suppress water peak. To perform ^1H NMR measurement, 800 uL of electrolyte sampled after CA tests was mixed with 100 uL DMSO standard solution (100 ppm) and 100 uL D_2O. Figure S14 showed the calibration curves of the liquid products, which was plotted by measuring standard solutions containing possible liquid products, including formate, acetate acid, methanol, ethanol, and 1-propanol. The faradaic efficiencies of liquid products were calculated as follows:

$$FE_l = \frac{Q_l}{Q_{total}} \times 100\% = \frac{n_l \times n \times F}{Q_{total}} \times 100\%$$

where n_l is the total content of certain liquid products in the catholyte, which was calculated by the concentration and the volume of the catholyte (20 mL). n is the number of electrons required to form the liquid products, and n = 2, 6, 8, 12 and 18 for formate, methanol, acetate, ethanol, and 1-propanol, respectively.

Declarations

Data availability

The data that support the findings of this study are available from the corresponding author on reasonable request.

References

1. Li M, Wang H, Luo W, Sherrell PC, Chen J, Yang J. Heterogeneous Single-Atom Catalysts for Electrochemical CO_2 Reduction Reaction. Adv Mater **32**, 2001848 (2020).

2. Ripatti DS, Veltman TR, Kanan MW. Carbon Monoxide Gas Diffusion Electrolysis that Produces Concentrated C_2 Products with High Single-Pass Conversion. Joule **3**, 240–256 (2019).

3. Zheng Y, Vasileff A, Zhou X, Jiao Y, Jaroniec M, Qiao S-Z. Understanding the Roadmap for Electrochemical Reduction of CO_2 to Multi-Carbon Oxygenates and Hydrocarbons on Copper-Based Catalysts. J Am Chem Soc **141**, 7646–7659 (2019).

4. Nitopi S, *et al.* Progress and Perspectives of Electrochemical CO_2 Reduction on Copper in Aqueous Electrolyte. Chem Rev **119**, 7610–7672 (2019).

5. Li CW, Ciston J, Kanan MW. Electroreduction of carbon monoxide to liquid fuel on oxide-derived nanocrystalline copper. Nature **508**, 504–507 (2014).

6. Li M, *et al.* Residual chlorine induced cationic active species on porous Cu electrocatalyst for highly stable electrochemical CO_2 reduction to C_{2+}. Angew Chem Int Ed **60**, 11487–11493 (2021).

7. Ross MB, *et al.* Designing materials for electrochemical carbon dioxide recycling. Nat Catal **2**, 648–658 (2019).

8. Li YC, *et al.* Binding Site Diversity Promotes CO_2 Electroreduction to Ethanol. J Am Chem Soc **141**, 8584–8591 (2019).

9. Chen C, *et al.* Cu-Ag Tandem Catalysts for High-Rate CO_2 Electrolysis toward Multicarbons. Joule **4**, 1688–1699 (2020).

10. Lv X, *et al.* Electron-Deficient Cu Sites on Cu_3Ag_1 Catalyst Promoting CO_2 Electroreduction to Alcohols. Adv Energy Mater **10**, 2001987 (2020).

11. Wang X, *et al.* Efficient upgrading of CO to C_3 fuel using asymmetric C-C coupling active sites. Nat Commun **10**, 5186 (2019).

12. Luo M, *et al.* Hydroxide promotes carbon dioxide electroreduction to ethanol on copper via tuning of adsorbed hydrogen. Nat Commun **10**, 5814 (2019).

13. Arán-Ais RM, Scholten F, Kunze S, Rizo R, Roldan Cuenya B. The role of in situ generated morphological motifs and Cu(I) species in C_{2+} product selectivity during CO_2 pulsed electroreduction. Nature Energy **5**, 317–325 (2020).

14. Calle-Vallejo F, Koper MTM. Theoretical Considerations on the Electroreduction of CO to C_2 Species on Cu(100) Electrodes. Angew Chem Int Ed **52**, 7282–7285 (2013).

15. Wang X, *et al.* Efficient electrically powered CO_2-to-ethanol via suppression of deoxygenation. Nature Energy **5**, 478–486 (2020).

16. Lum Y, Cheng T, Goddard WA, Ager JW. Electrochemical CO Reduction Builds Solvent Water into Oxygenate Products. J Am Chem Soc **140**, 9337–9340 (2018).

17. Ledezma-Yanez I, Gallent EP, Koper MTM, Calle-Vallejo F. Structure-sensitive electroreduction of acetaldehyde to ethanol on copper and its mechanistic implications for CO and CO_2 reduction. Catal Today **262**, 90–94 (2016).

18. Subbaraman R, *et al.* Trends in activity for the water electrolyser reactions on 3d M(Ni,Co,Fe,Mn) hydr(oxy)oxide catalysts. Nat Mater **11**, 550–557 (2012).

19. Kim J, *et al.* Tailoring binding abilities by incorporating oxophilic transition metals on 3D nanostructured Ni arrays for accelerated alkaline hydrogen evolution reaction. J Am Chem Soc **143**, 1399–1408 (2021).

20. Strmcnik D, *et al.* Improving the hydrogen oxidation reaction rate by promotion of hydroxyl adsorption. Nat Chem **5**, 300–306 (2013).

21. Clark EL, Hahn C, Jaramillo TF, Bell AT. Electrochemical CO_2 Reduction over Compressively Strained CuAg Surface Alloys with Enhanced Multi-Carbon Oxygenate Selectivity. J Am Chem Soc **139**, 15848–15857 (2017).

22. Kuhl KP, Hatsukade T, Cave ER, Abram DN, Kibsgaard J, Jaramillo TF. Electrocatalytic conversion of carbon dioxide to methane and methanol on transition metal surfaces. J Am Chem Soc **136**, 14107–14113 (2014).

23. Chen C, *et al.* Highly efficient electroreduction of CO_2 to C_{2+} alcohols on heterogeneous dual active sites. Angew Chem Int Ed **59**, 16459–16464 (2020).

24. Peterson AA, Nørskov JK. Activity descriptors for CO_2 electroreduction to methane on transition-metal catalysts. J Phys Chem Lett **3**, 251–258 (2012).

25. Luc W, Jiang Z, Chen JG, Jiao F. Role of surface oxophilicity in copper-catalyzed water dissociation. ACS Catal **8**, 9327–9333 (2018).

26. Kepp KP. A quantitative scale of oxophilicity and thiophilicity. Inorg Chem **55**, 9461–9470 (2016).

27. Moltved KA, Kepp KP. The chemical bond between transition metals and oxygen: electronegativity, d-orbital effects, and oxophilicity as descriptors of metal–oxygen interactions. The Journal of Physical Chemistry C **123**, 18432–18444 (2019).

28. Feaster JT, *et al.* Understanding Selectivity for the Electrochemical Reduction of Carbon Dioxide to Formic Acid and Carbon Monoxide on Metal Electrodes. ACS Catal **7**, 4822–4827 (2017).

29. Morimoto M, *et al.* Electrodeposited Cu-Sn Alloy for Electrochemical CO_2 Reduction to $CO/HCOO^-$. Electrocatalysis **9**, 323–332 (2018).

30. Wang P, *et al.* Phase and structure engineering of copper tin heterostructures for efficient electrochemical carbon dioxide reduction. Nat Commun **9**, 4933 (2018).

31. Huo S, *et al.* Coupled Metal/Oxide Catalysts with Tunable Product Selectivity for Electrocatalytic CO_2 Reduction. ACS Appl Mater Interfaces **9**, 28519–28526 (2017).

32. Schreier M, *et al.* Solar conversion of CO_2 to CO using Earth-abundant electrocatalysts prepared by atomic layer modification of CuO. Nature Energy **2**, 17087 (2017).

33. Ren W, *et al.* Isolated copper–tin atomic interfaces tuning electrocatalytic CO_2 conversion. Nat Commun **12**, 1449 (2021).

34. Ju W, *et al.* Sn-Decorated Cu for Selective Electrochemical CO_2 to CO Conversion: Precision Architecture beyond Composition Design. ACS Appl Energy Mater **2**, 867–872 (2019).

35. Liu J, *et al.* Facile preparation of a variety of bimetallic dendrites with high catalytic activity by two simultaneous replacement reactions. RSC Adv **3**, 14312–14321 (2013).

36. Li Z, *et al.* Highly Monodisperse Cu–Sn Alloy Nanoplates for Efficient Nitrophenol Reduction Reaction via Promotion Effect of Tin. Inorg Chem **59**, 1522–1531 (2020).

37. Zeng J, *et al.* Advanced Cu-Sn foam for selectively converting CO_2 to CO in aqueous solution. Appl Catal B: Environ **236**, 475–482 (2018).

38. Vasileff A, Xu C, Jiao Y, Zheng Y, Qiao S-Z. Surface and Interface Engineering in Copper-Based Bimetallic Materials for Selective CO_2 Electroreduction. Chem **4**, 1809–1831 (2018).

39. Sarfraz S, Garcia-Esparza AT, Jedidi A, Cavallo L, c K. Cu–Sn Bimetallic Catalyst for Selective Aqueous Electroreduction of CO_2 to CO. *ACS Catal* **6**, 2842–2851 (2016).

40. Morales-Guio CG, *et al.* Improved CO_2 reduction activity towards C_{2+} alcohols on a tandem gold on copper electrocatalyst. Nat Catal **1**, 764–771 (2018).

41. Wan W, Ammal SC, Lin Z, You K-E, Heyden A, Chen JG. Controlling reaction pathways of selective C–O bond cleavage of glycerol. Nat Commun **9**, 4612 (2018).

42. Lopes PP, Strmcnik D, Jirkovsky JS, Connell JG, Stamenkovic V, Markovic N. Double layer effects in electrocatalysis: The oxygen reduction reaction and ethanol oxidation reaction on Au(111), Pt(111) and Ir(111) in alkaline media containing Na and Li cations. Catal Today **262**, 41–47 (2016).

43. Subbaraman R, *et al.* Enhancing Hydrogen Evolution Activity in Water Splitting by Tailoring Li^+-$Ni(OH)_2$-Pt Interfaces. Science **334**, 1256–1260 (2011).

44. Choi C, *et al.* Highly active and stable stepped Cu surface for enhanced electrochemical CO_2 reduction to C_2H_4. Nat Catal **3**, 804–812 (2020).

45. Raciti D, *et al.* Low-overpotential electroreduction of carbon monoxide using copper nanowires. ACS Catal **7**, 4467–4472 (2017).

46. Luc W, *et al.* Two-dimensional copper nanosheets for electrochemical reduction of carbon monoxide to acetate. Nat Catal **2**, 423–430 (2019).

47. Bertheussen E, *et al.* Acetaldehyde as an Intermediate in the Electroreduction of Carbon Monoxide to Ethanol on Oxide-Derived Copper. Angew Chem Int Ed **55**, 1450–1454 (2016).
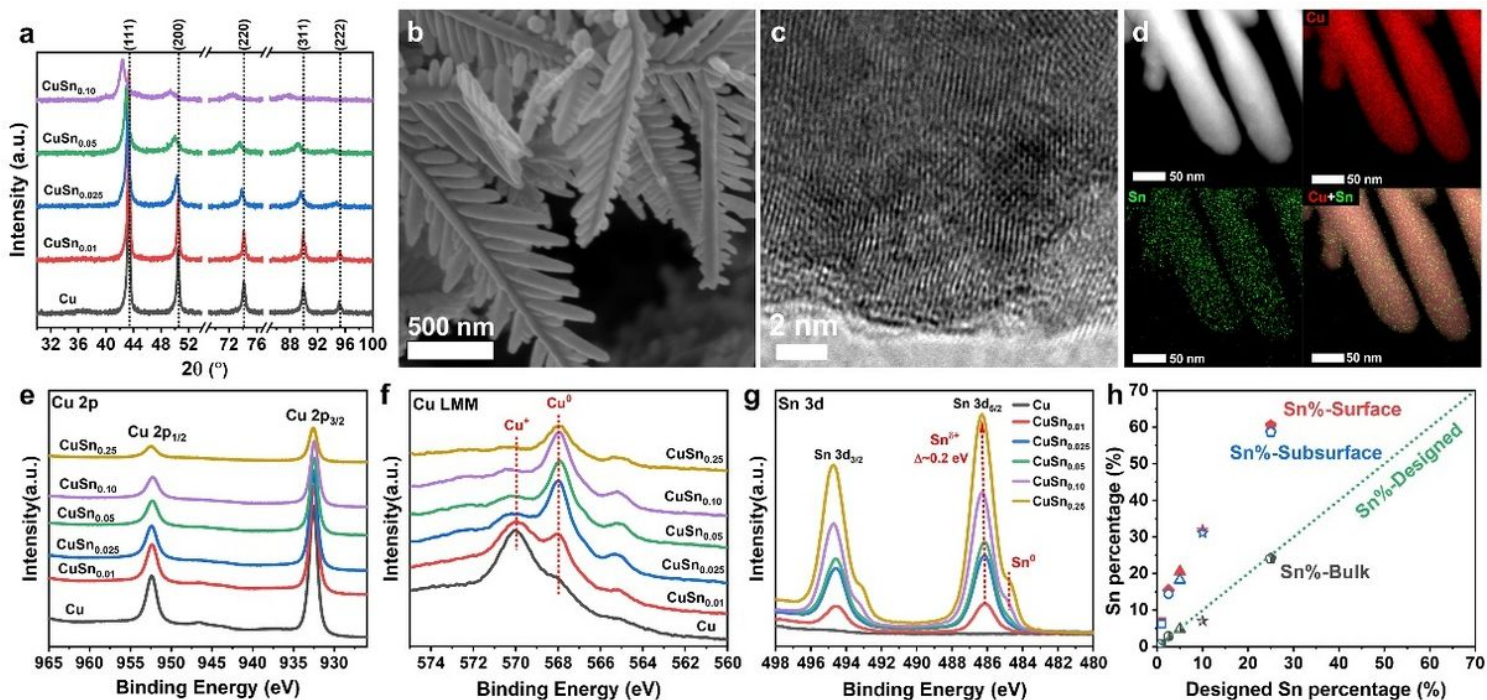
Figures

Figure 1

a The XRD patterns of $CuSn_x$ catalysts. **b** SEM image of $CuSn_{0.01}$ catalyst. **c** HR-TEM images of $CuSn_{0.01}$ catalyst. **d** HAADF-STEM images and EDS elemental mappings of $CuSn_{0.01}$ catalyst. **e** Cu 2p XPS spectra of $CuSn_x$ catalysts. **f** Cu LMM Auger spectra of $CuSn_x$ catalysts. **g** Sn 3d XPS spectra of $CuSn_x$ catalysts. **h** Bulk and surface composition characterized by EDS and XPS.
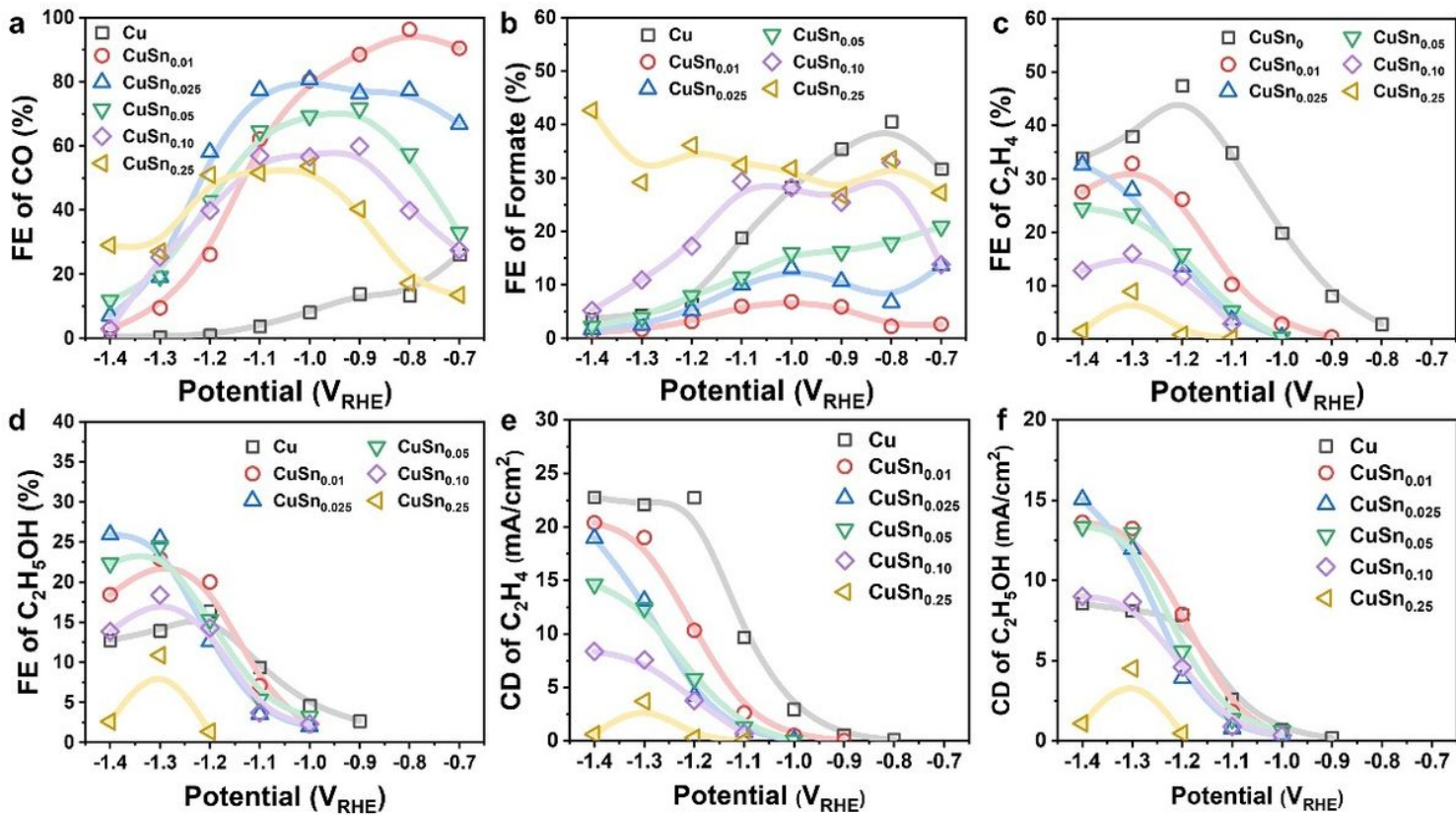
Figure 2

CO$_2$RR performance of CuSn$_x$. a FE of CO. **b** FE of formate. **c** FE of C$_2$H$_4$. **d** FE of C$_2$H$_5$OH. **e** Partial current density of C$_2$H$_4$. **f** Partial current density of C$_2$H$_5$OH.
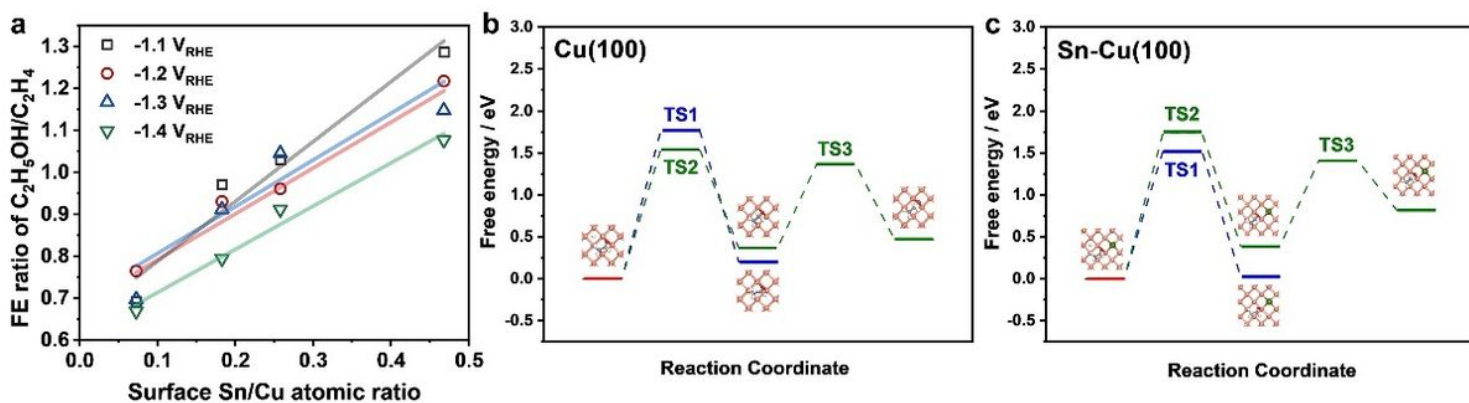
Figure 3

(a) FE of CO. (b) FE of formate. (c) FE of C$_2$H$_4$. (d) FE of C$_2$H$_5$OH. (e) FE ratios of C$_2$H$_5$OH/C$_2$H$_4$ at different potentials on CuSn$_x$ catalysts. (f) The correlation between surface Sn/Cu atomic ratio and FE ratio of C$_2$H$_5$OH/C$_2$H$_4$.
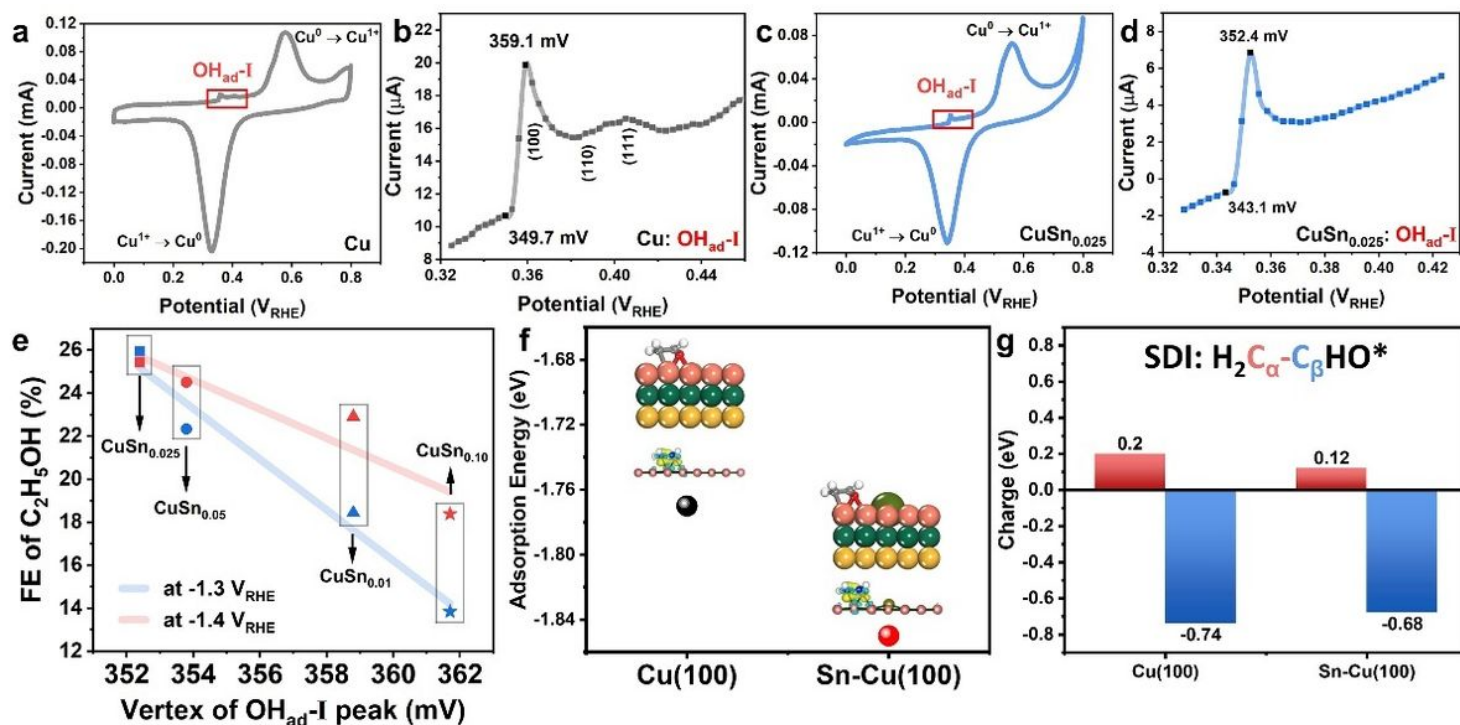
Figure 4

(a-b) CV curves of bare Cu catalyst. (c-d) CV curves of CuSn$_{0.025}$ catalyst. (e) CV curves of CuSn$_{0.01}$ catalyst. (f) CV curves of CuSn$_{0.05}$ catalyst. (g) CV curves of CuSn$_{0.10}$ catalyst. (h) CV curves of CuSn$_{0.25}$ catalyst. (i) The linear correlation of the oxophilicity of Cu sites with FEs of C$_2$H$_5$OH at -1.3 and -1.4 V$_{RHE}$.

Supplementary Files

This is a list of supplementary files associated with this preprint. Click to download.

- supplementalinformation0409.docx